Advancing Reconfigurable Manufacturing: Length-Adjustable Feed Axis and Stiffness-Adjustable Module for Modular Reconfigurable Machine Tools

Fabian Heimberger[a,*], Max Goebels[a], Jakob Janzen[a], Manuel Bader[a], Alexander Puchta[a], Florian Oexle[a], Jürgen Fleischer[a]

[a] *wbk Institute of Production Science, Karlsruhe Institute of Technology (KIT), Kaiserstraße 12, 76131, Karlsruhe, Germany*

Abstract

In today's manufacturing, rising demand for customized products and shorter product cycles challenges traditional systems, which adapt poorly to changing workspace needs and process dynamics. Reconfigurable manufacturing systems based on modular reconfigurable machine tools (MRMT) are promising, but current adaptability is mostly limited to swapping whole modules instead of tuning a single module's properties. This paper investigates the adaptation of two key MRMT properties at module level: the travel range of a feed axis and the chatter stability of a milling process. Two hardware demonstrators are used for this investigation: a length-adjustable rack-and-pinion feed axis that can be extended with attachable segments and a stiffness-adjustable interface that can vary static and dynamic stiffness via a preloaded spring plate. Laser-tracker measurements show that the travel range can be extended while keeping the maximum straightness deviation at 175.88 µm and rotational deviations within 0.1°. Static load tests yield stiffness ranges of 644.47 $\mathrm{N\,mm^{-1}}$ to 2089.35 $\mathrm{N\,mm^{-1}}$ (4 mm spring plate) and 694 $\mathrm{N\,mm^{-1}}$ to 2613.93 $\mathrm{N\,mm^{-1}}$ (5 mm spring plate), and impact-hammer tests show a shift of the dominant natural frequency of the module of 56.45 %. Stability lobe diagrams computed from the measured frequency response functions confirm that the module deliberately shifts the lobe positions along the spindle-speed axis, enabling in-situ adaptation of process stability limits.

Keywords: Machine tool, modular design, reconfiguration, feed drive, manufacturing, production

1. Introduction

Today's manufacturing companies are facing multiple challenges. Customers demand more personalized products, resulting in an increasing number of product variants with a decreasing number of units per product variant [1]. At the same time, product cycles are getting shorter [2]. To meet these increased demands and in order to produce at low production costs, next-generation production systems must be able to adapt more quickly and cost-effectively to new products [3].

Conventional manufacturing systems, such as dedicated manufacturing systems, cellular manufacturing systems and flexible manufacturing systems, are constrained in their adaptability to new products. This is particularly evident in instances where structural modifications to manufacturing machinery are required, such as when a larger workspace is necessary. Dedicated manufacturing systems are designed to produce specific products through rigid manufacturing processes with selected tools and fixed automation cycles. Therefore, with increasing product variants and fluctuating product volumes, dedicated manufacturing systems are losing their cost advantage [4]. Cellular manufacturing systems consist of machines grouped into several cells where each cell is able to produce for a specific part family and therefore offer some flexibility. However, since the relocation of cells and machines proves to be a time-consuming task, cellular manufacturing systems cannot respond quickly and cost-effectively to the demands of new products [5]. Flexible manufacturing systems consist of numerically controlled machines, an automated material handling system, and a centralized control for material and workpiece flow [6]. However, flexi-

*Corresponding author

Email address: fabian.heimberger@kit.edu (Fabian Heimberger)

ble manufacturing systems are only able to respond to product changes within a certain range, not to structural changes to the machines themselves, such as the need for a larger workspace [7].

In contrast to dedicated manufacturing systems, cellular manufacturing systems, and flexible manufacturing systems, Mühlbeier et al. present an alternative approach that uses standardized kinematics that allows the realization of entire value streams without the need for specialized machines [8]. Recent research has focused on implementing this approach using industrial robots as such standardized kinematic structures [9, 10]. However, industrial robots exhibit low stiffness and accuracy compared to machine tools [11]. Therefore, this approach exhibits significant limits regarding processes such as milling. As a result, there remains a need for machine tools that have the ability to change their process-specific characteristics, such as workspace or dynamics.

Software-defined manufacturing (SDM) is an innovative approach to manufacturing that emphasizes flexibility, collaboration, and the integration of digital technologies. Unlike the traditional production system-oriented model, SDM focuses on creating adaptive manufacturing solutions by using digital twins to map the physical behavior of machines in virtual space [12]. This enables machines to adapt to the specific requirements of the workpiece, whereas in conventional manufacturing the design of the workpiece is constrained by the capabilities of the machine on which it is to be manufactured. Additionally, SDM facilitates comprehensive digital planning and control, where physical processes align with digital specifications and machines are capable of autonomous decision-making [13, 14].

The SDM approach is extended by the concept of software-defined value stream process systems [15]. This novel concept extends SDM into production systems that are able to reconfigure themselves autonomously by establishing a cyber-physical chain. In this context, reconfigurable manufacturing systems are a promising solution as they offer significant potential for rapid and cost-effective adaptation to changing structural requirements while maintaining high productivity [16]. Reconfigurable manufacturing systems consist of modular reconfigurable machine tools (MRMT) that can be quickly reconfigured to meet changing structural requirements resulting from changing customer needs [16]. MRMT consists of basic and additional modules that can be assembled or disassembled as needed [17, 18]. The modules that satisfy the production specifications necessary to produce the workpiece are assembled into a kinematic structure. Extensive research has focused on enhancing MRMT through open standards, control architectures, algorithms, and optimization metrics [19], as well as methods on which modules to connect [20]. Existing research therefore largely treats the MRMT as module-based: adaptability is realized through the choice and arrangement of modules, not through changes inside a module itself. The question of how far these properties can be tuned within a single module, and what limits this intra-module adaptability imposes on the resulting machine behavior, has so far received little attention.

This paper addresses this gap by analyzing two such MRMT properties along two representative hardware modules:

- The *workspace* of a feed axis is studied on a length-adjustable rack-and-pinion axis whose travel range can be extended segment by segment. The analysis quantifies how the position-dependent straightness and rotational accuracy evolve along the assembled axis, and identifies the assembly interface as the dominating contributor.

- The *process stability* of a milling operation is studied on a stiffness-adjustable mechanical interface that varies the static and dynamic stiffness through the angular position of a preloaded spring plate. The analysis links the resulting shift of the dominant natural frequency to the chatter stability boundary by computing stability lobe diagrams from the measured frequency response functions.

The hardware modules themselves serve as analysis platforms; the focus of the paper is their resulting effect on MRMT properties.

This paper is structured as follows. Section 2 reviews the state of the art and the limitations of current solutions for workspace adaptation and chatter mitigation in MRMT. Section 3 derives the requirements that the two analysis platforms have to meet, and Section 4 describes their realization. The two-part analysis is then carried out in Section 5: accuracy along the extended travel range of the assembled feed axis and stiffness, frequency response, and stability lobe diagrams of the stiffness-adjustable interface. The implications of

these results for MRMT properties are discussed in Section 6, and the paper is concluded in Section 7.

2. State of the art

2.1. Length-adjustable feed axis

Lorenzer developed a MRMT that allows the axes to be interchangeable [21]. It is possible to choose between two axes of different predefined lengths: a short feed axis and a long one. If necessary, the axes can be reinforced through additional stiffening units. Although the workspace of the MRMT can be extended by replacing a short axis with a long one, the design of the axes does not allow the axis length to change at the module level, mainly due to the ball screw drive used. Bi developed a five-axis reconfigurable machine tool with a tripod-based parallel kinematic machine module and a serial kinematic linear XY table [22]. As with Lorenzer's approach, the machine's workspace is changed by swapping modules.

Peukert et al. identified hexagonal structures as suitable building blocks for modular machine tool frames [23]. Subsequently, Uhlmann et al. investigated how these hexagonal structures could be effectively connected to optimize stiffness, reliability, and cost [24]. Finally, Uhlmann and Peukert demonstrated that a modular machine tool frame based on hexagonal structures can achieve industry-relevant stiffness and process performance [25]. Although these hexagonal structures have been demonstrated as a structural foundation for length-adjustable feed axes [26], their broader adoption may face limitations due to the challenge of achieving precise alignment and motion control over long distances.

In soft robotics, there are different approaches that allow the synthetic growth of robot tips [27, 28], most prominently by eversion of material or by additive deposition of material at the tip [29]. Recent work also addresses the low stiffness of growing robots, for example with layer jamming that increases the bending stiffness by a factor of 4.6 [30]. However, even these stiffened designs are compliant structures without precise guidance and are therefore not suitable for use in MRMT.

In summary, none of the reviewed MRMT approaches provides a feed axis whose travel range can be extended at the module level while maintaining precise motion over the extended length.

2.2. Stiffness-adjustable module

Chatter vibration, such as regenerative chatter, is an example of self-excited vibration that occurs during the cutting process [31]. It manifests itself as undesired vibrations between the tool and the workpiece. The occurrence of this vibration is closely related to the noise level of the cutting forces, which is an external excitation. This type of vibration leads to numerous negative effects, such as poor workpiece surface quality, reduced accuracy, increased noise, and accelerated tool wear [32].

Among other factors, such as the geometry of the workpiece and the process parameters, chatter is mainly influenced by the dynamic behavior of the machine tool [31]. This dynamic behavior can be modeled using the principle of multiple single-mass oscillators whose mass, damping, and stiffness parameters can be modified. In particular, changing the mass or stiffness parameter of a single-mass oscillator causes its natural frequency to shift, thus affecting its dynamic behavior. This principle also applies to machine tools. Burtscher and Fleischer proposed a variable mass unit attached to the spindle housing to change the natural frequencies of the machine tool and thus reduce chatter [33]. While this method allows for adaptive tuning of the natural frequencies, it requires a complex setup.

Another way to change the natural frequencies of a machine tool is by changing the stiffness of specific modules or mechanical interfaces. Several methods exist that allow for a stiffness adjustment. Shape memory materials exhibit significant changes in their material properties when exposed to different temperatures. When exceeding a transition temperature T_{trans} their stiffness can be altered from hard ($T < T_{\text{trans}}$) to soft ($T > T_{\text{trans}}$) [34]. Wang et al. investigated changes in the dynamic behavior of a shape memory polymer joint [35]. They showed that resistive heating allows for a change in the stiffness of the joint, resulting in natural frequency shifts of up to 8.7 %. Although this concept shows promising results, precise temperature control is required to change the stiffness of the shape memory material accurately. Another approach to stiffness variation is to use nonlinear springs, which have a nonlinear relationship between force and spring deflection [36]. Although it is possible to implement this method through a simple design solution, the adjustable stiffness range is limited.

Yuan Lin et al. studied the effect of linear guide preload on the dynamic behavior of a vertical

column-spindle system [37]. The preload of the linear guides was shown to significantly affect the natural frequencies of the system. However, excessive preload can cause stick-slip behavior. This can reduce the smoothness of motion and affect the accuracy and precision of the system. In addition, high preload leads to higher friction caused by increased contact forces between the linear guide components. As a result, this can lead to an increased wear of components and an increase in energy consumption.

Hansmann et al. presented a simple design that allows precise stiffness adjustment for automotive applications, thus influencing the natural frequencies of these systems [38]. This is achieved by a mechanism that varies the preload applied to a spring plate. However, the design presented by Hansmann et al. is limited to unidirectional force transmission, which limits its application in MRMT, where both positive and negative directions in spatial axes must be accommodated. In addition, although this design allows some adjustment of the natural frequency, it is primarily limited to low-frequency eigenmodes, with a bandwidth of 137 Hz. Whereas for MRMT applications, frequency requirements typically range from 15 Hz to several thousand hertz [39, 40].

2.3. Aim of this work

The reviewed literature shows that workspace adaptation in MRMT is currently realized by exchanging entire fixed-length feed-axis modules [21, 22] or by reconfiguring frame structures, where precise motion control over extended distances remains an open issue [23, 24, 25, 26]. The first research question of this paper is therefore: *How does the accuracy of a MRMT feed axis evolve when its travel range is extended at the module level rather than by exchanging modules?* To answer this question, a variable-length rack-and-pinion feed axis with attachable extension segments is used as the analysis platform. The geometric and kinematic accuracy of the assembled axis is measured along the full travel range and decomposed into base-segment and extension-segment contributions in order to identify the dominating sources of deviation.

Likewise, existing approaches to adjust the dynamic behavior of machine tools to mitigate chatter face significant limitations such as complexity [33, 34, 35], limited stiffness adjustment range [36], or excessive preload that leads to wear and reduced accuracy [37]. The mechanism of Hansmann et al. [38] is a promising candidate but is limited to unidirectional force transmission and to a bandwidth of 137 Hz, whereas machine-tool applications require bidirectional force transmission and natural frequencies that range from 15 Hz to several thousand hertz [39, 40]. The second research question of this paper is therefore: *To what extent can the chatter stability of a milling process carried out on an MRMT be tuned by varying the stiffness of a single mechanical interface module?* To answer this question, a stiffness-adjustable interface module that extends the principle of Hansmann et al. to bidirectional force transmission and to the relevant machine-tool frequency range is used as the analysis platform. The static stiffness, the frequency response function and the resulting stability lobe diagram of a representative milling process are evaluated as a function of the angular position φ. This links the dynamic behavior of the module directly to the chatter stability boundaries of the process and thus to a tangible MRMT property.

3. Design considerations

3.1. Length-adjustable feed axis

Feed axes consist of a controller, an inverter, a motor, mechanical transmission elements, and measuring systems that work together to form a mechatronic control loop [41]. The following design focuses on the components of the mechanical transmission elements that are relevant to extending the travel range of the axis. The drive should be incrementally extendable, with no upper limit to the travel distance. Positioning accuracy and rigidity should be independent of the length of the axis. A ball screw drive traditionally used for milling applications proves to be unsuitable for an extension, as it is extremely difficult to attach extension pieces seamlessly and rigidly to the screw. In addition, the rigidity and accuracy of the screw decreases as the length of the screw increases. It is also necessary to avoid bending vibrations caused by the coincidence of the rotational frequency and the natural bending frequency in long spindles [41].

Another feasible option are linear drives, which can be chained together for a modular changeable length and feature both high accuracy and stiffness. However, they suffer from thermal issues, may require active cooling, and are more expensive and more complex overall [42].

The guide system must be selected in such a way that, when it is extended, uneven running of the

carriage is avoided when passing over the mechanical interfaces by the assembly of several guide rail sections. Rolling elements in commonly used recirculating ball bearing guides are highly sensitive to irregularities in the raceway [41]. As a result, rail sections must meet tight tolerances and be precisely aligned to allow for seamless extension when joining profiled rail sections. It is, therefore, necessary to select an alternative variant to meet these requirements. To ensure a smooth and accurate transition at the interconnection between two extension segments, a sufficiently rigid base structure must be provided to which the drive and guide components are aligned and fixed. The interconnections should be designed to allow for the accurate alignment of the extension segments. In addition, the interconnections should enable the axial bracing of the extension segments to provide sufficient stiffness while keeping the conversion effort minimal for quick reconfiguration.

3.2. Stiffness-adjustable module

As mentioned in Section 2.3, the design approach by Hansmann et al. presents a promising foundation to reach the intended goals. Therefore, this paper further develops this approach. The aim is to adapt and expand the design to meet the specific requirements of MRMT. The stiffness adjustment should function bidirectionally, necessitating bidirectional force flow through the module. A key objective is to shift the MRMT's natural frequencies through stiffness changes to optimize performance and vibrational properties. Given that the original design reaches a maximum natural frequency of 137 Hz, this approach will be further developed to achieve frequencies in the range typical for machine tool applications (15 Hz to several thousand hertz [39, 40]). In addition, the main contribution should lie in enabling bidirectional force transmission in both spatial directions to meet MRMT requirements.

4. Design

4.1. Length-adjustable feed axis

The length-adjustable feed axis is designed as a rack and pinion drive system to combine stiffness and modularity. The basic structure of the length-adjustable feed axis consists of two parallel aluminum profiles connected by a plate. As shown in Figure 1 slot nuts are installed in pairs at the end faces of the aluminum profiles in the grooves, allowing the extension segments to be connected in alignment. Additional bolt connectors provide axial tension to increase axial stiffness. The linear guide consists of two parallel T-guide rails, each with two slide bearing carriages, connected by a carriage plate. A fixed/floating bearing arrangement is realized by using fixed bearings on one side and floating bearings on the other side of the carriage plate. The reason for choosing a sliding linear guide is the larger surface contact compared to roller bearings, which, in combination with the slightly chamfered guide rail sections at the end faces, should allow smooth running over the guide rail joints. A rack and pinion drive was chosen because it allows the travel path to be easily extended to any length by attaching additional rack sections. Additionally, unlike ball screw drives, the rigidity is independent of the length of the travel path [41]. To avoid producing an accuracy error at the transition between two rack sections, the gap between two rack pieces is established using an assembly gauge, a short toothed rack piece that meshes with the teeth of both adjacent rack sections and thus sets the correct tooth pitch across the transition [43]. As the interfaces of the rack and linear guide rail sections are not designed to be flush with the interfaces of the base plate, the rack and guide rail sections can always be attached to two sections, which adds additional rigidity. Torque and speed are transmitted via a planetary gearbox that connects the pinion and the motor.

4.2. Stiffness-adjustable module

The design proposed in this paper builds on the principle of an adjustable spring element presented by Hansmann et al. and extends its capabilities towards bidirectional force transmission in opposite spatial directions [38] (see Section 3.2). The adjustable spring element is based on a spring plate, which is attached to two structures by several connection pins, as illustrated in Figure 2. One structure remains fixed (fixed structure), while the other structure is rotatable (rotatable structure). The resulting stiffness in the z-direction is determined by the angular position φ of the connection pins of the two structures relative to each other. At an angular position of $\varphi = 0°$, all connection pins mounted on the fixed structure are perfectly aligned with the connection pins on the rotatable structure. The spring plate is, therefore, fixed into place and is

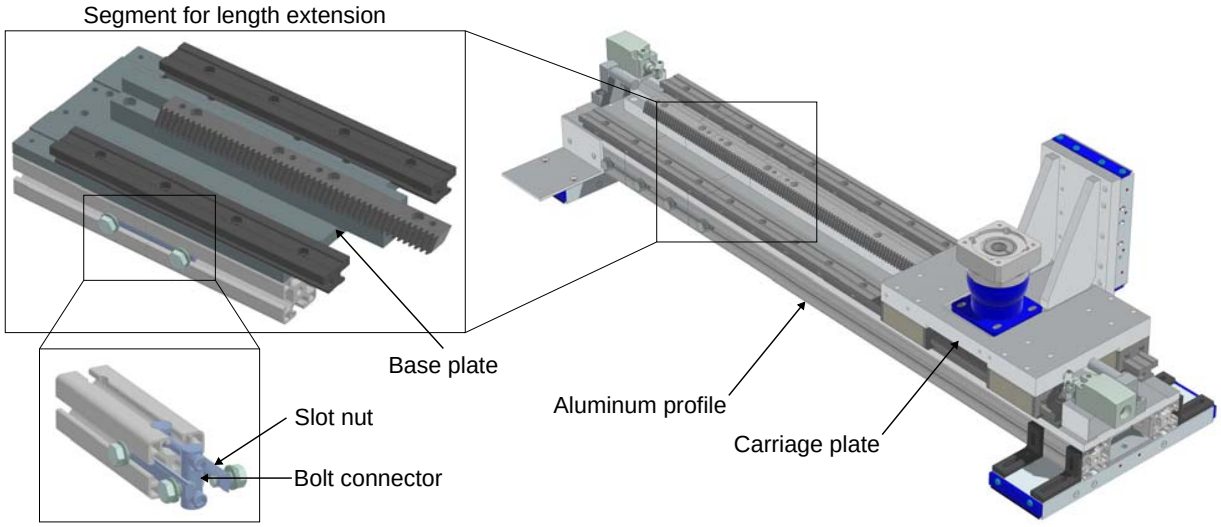


Figure 1: Overview of the complete feed axis with two extension segments.

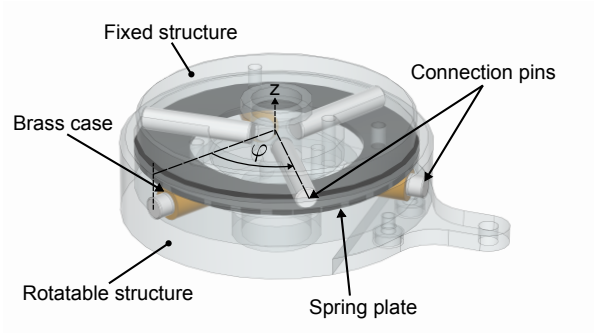


Figure 2: Working principle of the stiffness-adjustable module – The angle φ between the connection pins can be changed by rotating the fixed and the rotatable structure relative to each other. This changes the preload of the spring plate and, thus, the stiffness in the z-direction.

not able to move in the z-direction. At this position, the module achieves its maximum stiffness. To reduce the stiffness of the module, the angular position φ is increased by rotating the rotatable structure relative to the fixed structure. As shown in Figure 2, increasing the angular position causes the connection pins of the two structures to become misaligned. This misalignment reduces the effective stiffness of the stiffness-adjustable module. Specifically, the stiffness now depends on the angular position φ, as this determines the portion of the spring plate that is able to move freely. It is important to note that adjusting the angular position φ does not affect the height of the stiffness module, provided no external forces are applied in the z-direction.

In the design proposed in this paper, the connection pins are mounted in two housings using cylindrical pins. To reduce friction when changing the angular position, brass cases are fitted on the cylindrical pins attached to the rotatable structure. As shown in Figure 3, for compression forces F_p, the force is transmitted from one housing to the other via the spring plate. In the case of tensile forces

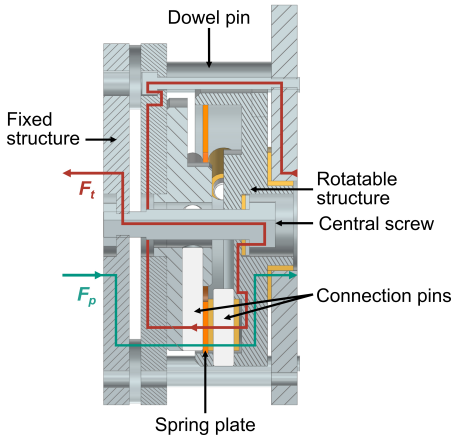


Figure 3: Section view of the stiffness-adjustable module with force flow. Compressive forces F_p (marked green) are transferred directly through the spring plate to the other side of the module. Tensile forces F_t (marked red) are transferred to the spring plate through a central screw and then to the other side of the module via additional screws.

F_t, the force is transmitted through a central screw to the spring plate and then to the fixed structure,

as shown in the force flow in Figure 3. This allows the stiffness to be modified both in the positive and negative X-directions of the MRMT. The module is designed to accommodate a maximum load of 5 kN. The spring plate is constructed using multiple 0.5 mm thick spring steel disks, allowing a wide stiffness range that can easily be tailored to specific requirements (see Section 6.2). The lateral forces generated during the milling process are captured by linear guides, which are realized with dowel pins and straight linear plain bearings. The stiffness of the module can automatically be adjusted using a linear actuator connected to the rotatable structure. In addition, it is also feasible to change the stiffness using a rotary actuator.

5. Results

The two research questions formulated in Section 2.3 are now addressed experimentally. Section 5.1 quantifies how the accuracy of the MRMT feed axis evolves along an axis assembled from a base segment and two extension segments. Section 5.2 then quantifies how the static stiffness, the dynamic response and the chatter stability boundary of a milling process change with the angular position φ of the stiffness-adjustable interface module.

5.1. Length-adjustable feed axis

Because the travel range is extended by adding segments, the resulting interfaces may compromise the geometric accuracy of the axis. This subsection quantifies the straightness and angular deviations of the carriage motion over the extended travel.

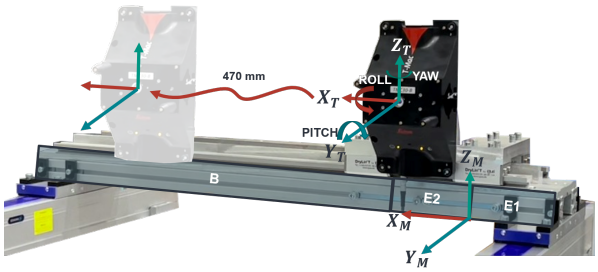


Figure 4: Experiment setup for measuring the straightness deviation of the length adjustable feed axis using a 6DOF laser tracker target. The index M denotes the fixed machine coordinate system, the index T the coordinate system of the laser tracker target moving with the carriage. The straightness and rotatory deviations along the axis X_M are measured.

A Leica AT960MR laser tracker is used for the straightness deviation test (see Figure 4). A 6-degree-of-freedom (DOF) laser tracker target is mounted on the axis carriage plate. The axis, assembled from the base segment B and the two extension segments E1 and E2 (see Figure 1), is driven from a starting position of 0 mm in axis coordinates to a final position of 470 mm at different speeds of $50\,\mathrm{mm\,s^{-1}}$, $250\,\mathrm{mm\,s^{-1}}$, $500\,\mathrm{mm\,s^{-1}}$ and $600\,\mathrm{mm\,s^{-1}}$. For each speed, six measurements are taken: three during the forward movement of the carriage and three during the reverse movement of the carriage. For each direction of travel, the three runs are interpolated piece-wise linearly onto common sample points to avoid sampling errors, and the point-wise mean and standard deviation σ across the runs are then computed. In our measurement setup, the 0 mm position corresponds to the center of the carriage of the MRMT being at its end-stop. As shown in Figures 4 and 5, at this position, the outermost slide carriages, which are mounted on the carriage plate (see Figure 1), are approximately centered over the gap between the extension segments E1 and E2. Critical positions where deviations may occur are when the center of the carriage plate is fully positioned on the middle extension segment E2 when the pinion crosses the gap between the jointed racks, or when the carriage transitions between extension segment E2 and the long base segment B. Positioning and rotational deviations (D, Yaw, Pitch, Roll) along the axis are measured with the laser tracker, with the primary metric being the least squares deviation between a nominal line and the measured trajectory. To show possible deflections due to shifts in the interfaces between the extension segments, a nominal line is calculated using measurement points taken along the large base segment B in the direction of X_M. As a result, positioning errors in X_M direction cannot be measured and only deflections in Y_T, Z_T are considered. In the terminology of ISO 230 [44, 45], the quantities evaluated here therefore belong to the geometric accuracy of ISO 230-1 rather than to the positioning accuracy of ISO 230-2. The deviation D in Y_T/Z_T is the straightness deviation of the carriage motion (the linear error motions E_{YX} and E_{ZX}), while Yaw, Pitch and Roll are the angular error motions E_{CX}, E_{BX} and E_{AX}. The bidirectional positioning parameters of ISO 230-2 – positioning uncertainty A, repeatability R, systematic deviation E, reversal value B and mean bidirectional deviation M – require target-position

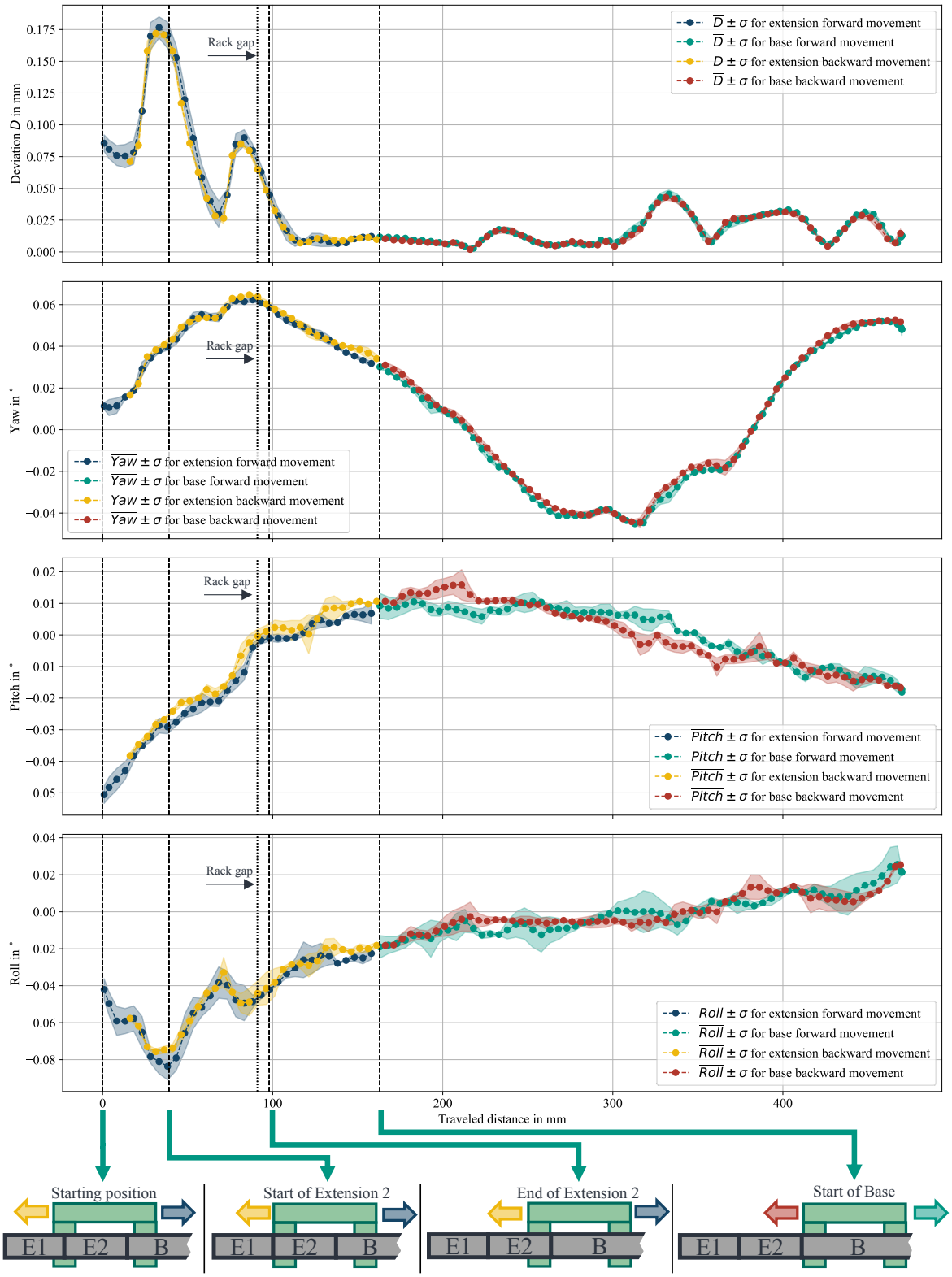


Figure 5: Straightness and rotatory deviation of the length adaptable axis in forward and backward motion and speed of $50\,\mathrm{mm\,s^{-1}}$. $\overline{\cdot}$ denotes the mean, σ denotes standard deviation. The plotted deviation D is the straightness deviation of the carriage motion in Y_T/Z_T (linear error motions E_{YX}, E_{ZX}, ISO 230-1).

measurements along the travel direction X_M and are outside the scope of this evaluation; the forward/backward consistency is instead characterized globally by the Normalized Root Mean Squared Error (NRMSE) defined below.

The laser tracker provides the rotation data as quaternions at the sampled time steps; for readability, all rotations are reported as intrinsic Tait-Bryan angles $Z_T - Y'_T - X''_T$ (yaw, pitch, roll). Two coordinate systems must be considered (see Figure 4): the fixed machine coordinate system (X_M, Y_M, Z_M) and the moving coordinate system of the laser tracker target (X_T, Y_T, Z_T). For zero rotation the two systems are parallel ($X_T \parallel X_M$, $Y_T \parallel Y_M$, $Z_T \parallel Z_M$); nonzero rotation corresponds to a deviation from this parallelism.

At the measurement distance of 2 m in this setup, the maximum permissible error (MPE) of the laser tracker for positioning deviations is 27 µm, calculated from the specified MPE of $15\,\mu m + 6\,\mu m\,m^{-1}$. The MPE for rotation is 0.01° [46].

The straightness deviation results for a speed of $50\,mm\,s^{-1}$ are shown in Figure 5. At the higher speeds of $250\,mm\,s^{-1}$, $500\,mm\,s^{-1}$ and $600\,mm\,s^{-1}$, the measurements show basically identical behavior, only sampled more coarsely, and are therefore not shown separately. For comparison, the average straightness deviation $\overline{D}$ over all measurement runs for each forward and backward movement, as well as the corresponding standard deviations σ, are plotted separately for the base and extension segments. Note that the length of the carriage plate is twice the length of a single extension segment. This is important because it smooths out the deviations in straightness deviation. The standard deviations across all measurements do not exceed $\sigma = 10.56\,\mu m$, which is below the MPE. The run-to-run variation can therefore not be separated from the measurement uncertainty, and the repeatability of the axis is at least as good as this value. The straightness deviations themselves, of up to 175.88 µm, exceed the MPE by a factor of about 6.5 and are thus clearly attributable to the axis. The measurements show consistent results for both forward and backward movement of the carriage (see Figure 5). Quantitative validation of this observation is provided by the NRMSE,

$$\mathrm{NRMSE} = \frac{\mathrm{RMSE}}{\max(\overline{D_\mathrm{f}}) - \min(\overline{D_\mathrm{f}})},$$

$$\mathrm{RMSE} = \sqrt{\frac{1}{N}\sum_{i=1}^{N}\left(\overline{D_{\mathrm{f},i}} - \overline{D_{\mathrm{b},i}}\right)^2}$$

where $\overline{D_{\mathrm{f},i}}$ denotes the mean position deviation in forward direction at sample point i, $\overline{D_{\mathrm{b},i}}$ the corresponding value in backward direction, $\max, \min$ denote the maximum and minimum values respectively and N denotes the sample size. The NRMSE between forward and backward runs is 0.0236. Straightness deviation variations observed in the base segment of the feed axis range from 2.05 µm to 44.5 µm. These variations are due to manufacturing and assembly issues and are not specific to the length-adjustable design. The straightness deviation of the extension segments varies from 6.76 µm to 175.88 µm. The straightness deviation over the extension segments shows a sinusoidal behavior with two peaks at 175.88 µm (forward movement) and 89.65 µm (forward movement). The observed peak-to-peak distances correspond to the length of one extension segment.

The recorded measurement results indicate that the rotational components roll, pitch, and yaw generally remain within an order of magnitude of 0.1°. The standard deviations observed in the measurements (run-to-run repeatability across the three repetitions) are below 0.01°, which is within the MPE of the measurement setup. A significant fluctuation in the yaw angle was observed for the base segment B (Max – Min = 0.101°), which is markedly larger than for the extension segments (Max – Min = 0.056°). The pitch behavior differs between the two segments: pitch decreases noticeably along the traveled distance within the base segment B, while it increases along the traveled distance within the extension segments. A direct comparison between the base segment B and the extension segments highlights the role of assembly precision and manufacturing constraints: within the base segment B, a variation of Max – Min = 0.042° can be observed, whereas the extension segments exhibit a larger variation of Max – Min = 0.068°, i.e. approximately 62 % worse. Evaluation of the roll measurements provides further insight into the alignment quality of the system. The roll values within the base segment B vary by Max – Min = 0.07°. For the extension segment E2, which is fully traversed

over a traveled distance of 39 mm to 98 mm, a variation of Max – Min = 0.041° is observed. For the extension segment E1, which is only partially traversed (0 mm to 39 mm and 98 mm to 163 mm combined), a larger variation of Max – Min = 0.062° is observed. The total variation over both extension segments combined is likewise Max – Min = 0.062° (set by E1), indicating that alignment deviations accumulate across the segment interfaces.

5.2. Stiffness-adjustable module

Two different types of tests are performed to validate changes in static stiffness and dynamic behavior in terms of natural frequency shifts as a function of angular position φ.

First, the change in static stiffness as a function of the angular position $\varphi \in \{10°, 20°, 30°, 40°, 50°, 60°\}$ is measured. A static compression load of 5 kN is applied to the stiffness-adjustable module in the z-direction using a hand press. This load corresponds to the nominal load of the module. The force applied to the module is measured using a Burster 8524-6005 compression load cell, and the displacement is measured using a Burster 8709-5100 potentiometric displacement sensor. Three experiments are performed for each angular position, and then the measurements are averaged. Thus, inaccuracies in manual force application, as well as measurement inaccuracies, are minimized. In addition, the measurements are performed for different thicknesses $T = \{4\,\text{mm}, 5\,\text{mm}\}$ of the spring plate to study this influence as well.

The results of the static stiffness experiments are shown in Figure 6. It can be observed that

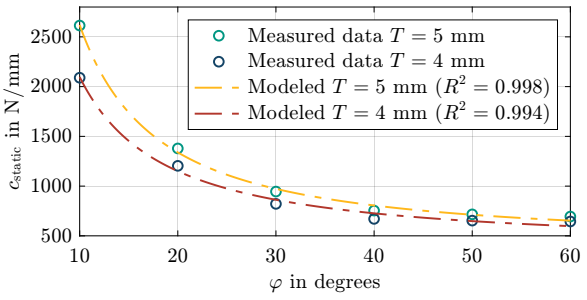


Figure 6: Measured static stiffness (compression) values of the stiffness-adjustable module for different angle settings φ and spring plate thicknesses T.

for a constant thickness T of the spring plate, the static stiffness decreases with increasing angular position φ. The static stiffness values for $T = 4\,\text{mm}$ vary between $2089.35\,\text{N mm}^{-1}$ at $\varphi = 10°$ and $644.47\,\text{N mm}^{-1}$ at $\varphi = 60°$. For a spring plate thickness of $T = 5\,\text{mm}$, the stiffness values range from $2613.93\,\text{N mm}^{-1}$ at $\varphi = 10°$ to $694\,\text{N mm}^{-1}$ at $\varphi = 60°$.

Impact hammer tests are performed to evaluate the changes in the dynamic behavior of the stiffness-adjustable module as a function of the angular position φ. The impact hammer tests are performed only for the spring plate thickness configuration $T = 5\,\text{mm}$. The test setup is as follows: The module is clamped to a machine table using a machine vice. The module is excited on its upper side with a Kistler 9726A20000 quartz impulse force hammer in the operating direction of the spring plate (z-axis of the module, see Figure 3), and the force excitation is measured. The system response is measured with a PCB-356A33 triaxial accelerometer mounted on top of the structure of the stiffness module that can move freely and is not clamped by the machine vice.

Figure 7(a) shows the measured frequency response functions (FRFs) for all six angular positions. A clear shift of the resonance with the angular position is visible; the frequency of the module mode identified below is marked by dashed vertical lines. In the range around these frequencies the coherence exceeds 0.8 at every angular position, so that according to Goldman the measurements can be considered usable [47]. Towards the upper end of the measured band the coherence degrades; for $\varphi = \{20°, 40°, 50°\}$ it no longer reaches 0.8 above approximately 240 Hz to 290 Hz, which sets the upper limit of the evaluation. All frequencies of the module mode lie below this limit.

For each angular position $\varphi \in \{10°, 20°, 30°, 40°, 50°, 60°\}$, the module is excited in the z-direction and the response is recorded in all three directions of the triaxial accelerometer, which yields three FRFs per angular position with a common reference. Natural frequencies, damping ratios and complex mode shapes are extracted from these measurements using the least-squares complex frequency-domain estimator PolyMAX [48], which returns an unordered set of 6 to 13 poles per angular position. Because the response is measured at a single location, each mode shape is a three-component vector: it characterizes the direction in which a mode moves, but not its spatial distribution over the structure. The FRF

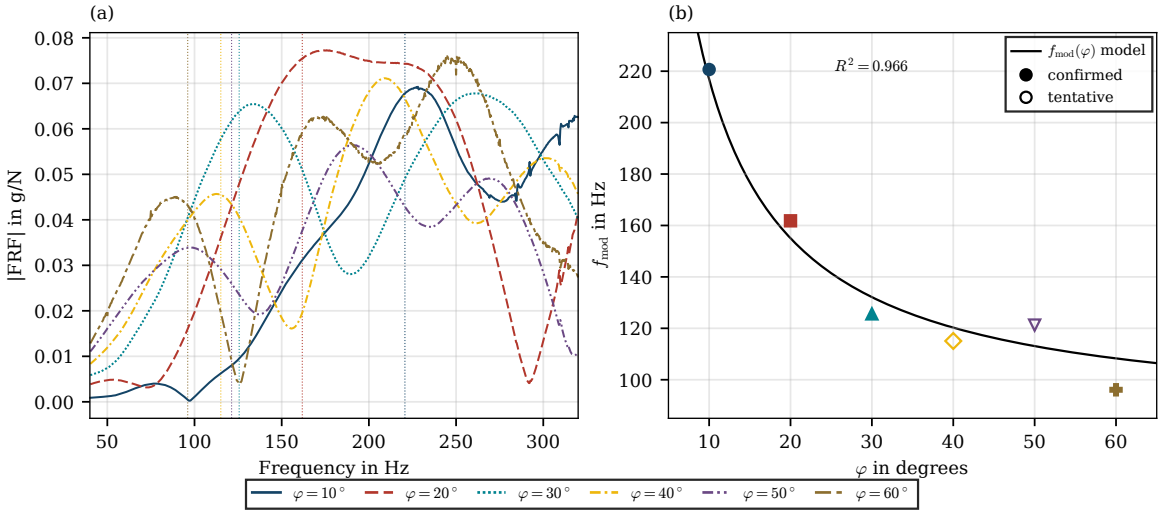


Figure 7: Dynamic behaviour of the stiffness-adjustable module for a spring plate thickness of $T = 5\,\mathrm{mm}$. (a) FRFs measured at the six angular positions φ; the dashed vertical lines mark the frequency f_{mod} of the identified module mode. (b) f_{mod} as a function of φ. The solid line is the single-parameter model $f_{mod}(\varphi) = f_s\sqrt{c_{\mathrm{static}}(\varphi)/c_{\mathrm{static}}(\varphi_{\mathrm{ref}})}$ derived from the static stiffness model of Figure 6, with $f_s = 120.26\,\mathrm{Hz}$, $\varphi_{\mathrm{ref}} = 40°$ and $R^2 = 0.966$. Open symbols at $\varphi = 40°$ and $\varphi = 50°$ mark the settings of increased identification uncertainty discussed in the text.

measured in the direction of the applied force, shown in Figure 7(a), is the one used for the stability analysis in Section 5.2.1.

The measured structure comprises not only the module but also the machine vice and the machine table to which it is clamped, so the identified poles include modes of the surrounding setup. Neither their number nor their ordering by frequency is preserved across φ, and the module mode can therefore not be selected at each angular position in isolation. It has to be identified as a chain, that is, a selection of one pole per angular position. With the given pole counts, 316,800 chains can be formed, of which only one represents the module mode while all others mix poles belonging to different modes. Building the chain incrementally, by tracking the mode shape from one angular position to the next, is not reliable here: the frequency of the module mode changes by more than a factor of two over the adjustment range and therefore crosses several other poles of the structure, so that a single local decision propagates into all subsequent ones. The chains are therefore evaluated as a whole.

The primary selection criterion is derived from the static stiffness measurements of Figure 6 and is thus independent of the modal data. For a single-degree-of-freedom oscillator, the natural frequency is

$$f = \frac{1}{2\pi}\sqrt{\frac{c_{\mathrm{static}}}{m}}$$

Changing the angular position φ alters which portion of the spring plate is free to deflect, but not the mass of the freely moving part of the module, so m can be assumed independent of φ while the modal stiffness k is proportional to the measured static stiffness $c_{\mathrm{static}}(\varphi)$. The frequency of the module mode is then expected to follow

$$f(\varphi) = f_s\sqrt{\frac{c_{\mathrm{static}}(\varphi)}{c_{\mathrm{static}}(\varphi_{\mathrm{ref}})}}$$

where φ_{ref} is an arbitrary reference angle. The scaling parameter f_s absorbs everything the static measurement does not determine, namely the modal mass and the ratio between the statically measured stiffness and the modal stiffness of the mode. The shape of the curve over φ is therefore fixed by the static measurement, and its absolute level is the only free parameter. Each of the 316,800 chains is fitted in this way and rated by its coefficient of determination R^2.

This criterion is selective: only 6 of the 316,800 chains reach $R^2 \geq 0.95$, and only 25 reach $R^2 \geq 0.90$. Within these few candidates, however, the differences in R^2 are of the order of 0.002. A de-

cision based on R^2 alone would not be meaningful, so a second, independent criterion is applied.

The second criterion is the z-dominance of the mode shape, defined as the fraction of the mode shape acting in the z-direction. It follows directly from the design of the module: the compliance introduced by the spring plate acts in the z-direction only, whereas lateral forces are carried by the linear guides described in Section 4.2. A mode belonging to the module must therefore move predominantly in z, while modes of the vice and the machine table have no reason to do so. Since the z-dominance is evaluated from the mode shapes and the frequency criterion from the static stiffness measurement, the two criteria are independent of each other. The selected chain is not the one with the highest $R^2 = 0.968$. That chain was discarded because its mode shapes are only weakly z-dominant, with a minimum of 0.55 across the six angular positions. The selected chain reaches a minimum z-dominance of 0.72 at a marginally lower $R^2 = 0.966$.

Figure 8 shows all 61 identified poles. Besides the six poles forming the module mode, two clusters remain nearly constant over φ. The first, at

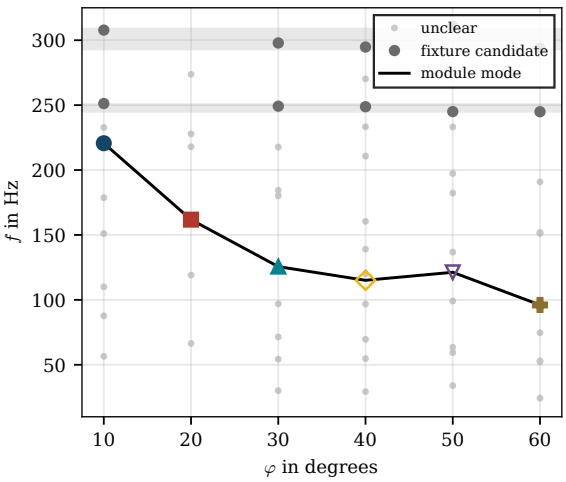


Figure 8: All 61 poles identified at the six angular positions. The module mode forms a chain whose frequency varies by more than a factor of two over φ, whereas the two pole clusters near 248 Hz and 301 Hz remain nearly constant and are attributed to the machine vice and the machine table. Poles without a consistent assignment across angular positions are shown in grey.

approximately 248 Hz, occurs at five of the six angular positions and varies by less than 3 Hz; as it does not follow the stiffness trend, it is attributed to the vice and the machine table. The second, near 301 Hz, is more scattered and lies above the coherence limit identified above at four of the five angular positions at which it appears, so that its parameters are less reliable; it is likewise excluded. The remaining 45 poles cannot be assigned consistently across angular positions. Among them are poles below the module mode, between 24 Hz and 66 Hz, present at every angular position. They are not z-dominant, show no consistent mode shape across φ, and do not follow the stiffness trend ($R^2 = 0.55$ against the same one-parameter model, compared with $R^2 = 0.966$ for the module mode). They are therefore not attributable to the module; their effect on the stability boundary is addressed in Section 5.2.1.

Figure 7(b) shows the frequency f_{mod} of the identified module mode as a function of the angular position; the corresponding modal parameters are summarized in Table 1.

Table 1: Modal parameters of the identified module mode for $T = 5$ mm. c_{static} is the independently measured static stiffness (Figure 6), ζ the damping ratio, and z-dom. the fraction of the mode shape acting in the operating direction of the spring plate. The Modal Assurance Criterion (MAC) refers to the pair formed by the given setting and the next larger φ; since the response was measured at a single location, the mode shapes have three components, so a MAC of about 1/3 corresponds to unrelated shapes. Δf is the deviation from the single-parameter model $f_{\mathrm{mod}}(\varphi) = f_{\mathrm{s}}\sqrt{c_{\mathrm{static}}(\varphi)/c_{\mathrm{static}}(\varphi_{\mathrm{ref}})}$ with $f_{\mathrm{s}} = 120.26$ Hz.

φ [°]	c_{static} [N mm^{-1}]	f_{mod} [Hz]	ζ [%]	z-dom. [–]	MAC [–]	Δf [%]
10	2619.5	220.66	14.9	0.72	0.36	+1.8
20	1338.8	161.81	32.2	0.96	0.84	+4.4
30	972.5	125.62	26.3	0.98	0.75	−4.9
40	805.7	115.07	11.4	0.81	0.36	−4.3
50	712.2	121.25	14.5	0.75	0.58	+7.2
60	653.1	96.09	17.6	0.97	–	−11.3

For a spring plate thickness of $T = 5$ mm, f_{mod} decreases from 220.66 Hz at $\varphi = 10°$ to 96.09 Hz at $\varphi = 60°$, a shift of 56.45 % over the adjustable range. Consistent with the single degree of freedom (SDOF) hypothesis used for the identification, the frequency is described not by an independent three-parameter regression but by scaling the static stiffness model of Figure 6, with a single free parameter $f_{\mathrm{s}} = 120.26$ Hz and an arbitrary reference angle $\varphi_{\mathrm{ref}} = 40°$. The model reproduces the six measured frequencies with $R^2 = 0.966$, with deviations listed in the last column of Table 1 that

reach 11.3 % at $\varphi = 60°$. The reported shift is sensitive to this last value: had $f_{\mathrm{mod}}(60°)$ followed the model exactly, the shift would amount to 50.9 % rather than 56.45 %. Since the same trend was used to select the mode, this agreement quantifies the internal consistency of the identification rather than confirming it independently; the independent evidence for the selected chain is the z-dominance listed in Table 1. The MAC values given alongside are computed from three-component mode shapes and therefore have limited discriminating power, since a value of about 1/3 is already expected for unrelated shapes. They support the continuity of the chain at three of its five transitions. As a plausibility check, back-calculating an equivalent modal mass from $m = c_{\mathrm{static}}(\varphi)/(2\pi f_{\mathrm{mod}})^2$ yields a median of 1.46 kg, which is the expected order of magnitude for the freely moving part of the module.

The damping ratios in Table 1 are high, between $\zeta = 11.4\,\%$ and $\zeta = 32.2\,\%$, compared with the 1 % to 5 % typical of machine tool structures. This is consistent with frictional dissipation in the preloaded pin-to-spring-plate contacts through which the module transmits load. It broadens the resonance peaks, so that individual pole frequencies are resolved with correspondingly lower accuracy, and it affects the stability boundary evaluated in Section 5.2.1.

Two observations qualify the frequency trend. First, it is not strictly monotonic: the value at $\varphi = 50°$ lies 5.4 % above the value at $\varphi = 40°$, although the static stiffness decreases monotonically over the entire range. Second, the mode shapes are least clean at exactly these two settings: the z-dominance falls to 0.81 and 0.75, compared with 0.96 to 0.98 at $\varphi = 20°$, 30° and 60°, and the two MAC values adjoining $\varphi = 40°$ drop to the level expected for unrelated shapes (Table 1). Both observations are consistent with a curve-veering interaction, in which the module mode approaches a further structural mode in the range $40° \leq \varphi \leq 50°$ and exchanges shape content with it, so that it departs locally from the stiffness-governed trend. The frequencies at these two settings therefore carry a higher identification uncertainty than the remaining four, whereas the overall trend and the two end points of the adjustment range are unaffected.

The stability of the identification was assessed by resampling the parameters of the static stiffness fit 100 times from their covariance matrix and repeating the complete selection. The same chain is obtained in 83 % of the resamples, and the assignment at $\varphi = 60°$ in 98 %. The dominant alternative, accounting for 15 of the 17 deviating cases, is inferior in every criterion when evaluated against the original stiffness fit ($R^2 = 0.948$, minimum z-dominance 0.35, MAC between 0.20 and 0.63) and is therefore regarded as an artefact of the uncertainty in the stiffness fit parameters rather than as a competing interpretation.

5.2.1. Process-side evaluation: stability lobe diagrams

The shift of the natural frequency demonstrated above directly translates to a change in the chatter stability boundary of a milling process. To quantify this effect, stability lobe diagrams (SLDs) are computed from the measured FRFs for each of the six angular positions $\varphi \in \{10°, 20°, 30°, 40°, 50°, 60°\}$ using the Fourier-series-based analytical method introduced by Altintas and Budak [49]. In this method, the time-varying directional dynamic milling coefficients are expanded in a Fourier series and truncated. The limiting axial depth of cut a_{lim} as a function of spindle speed n is then obtained from the oriented FRF together with the specific cutting force coefficients and the force angle of the tool-workpiece pair.

It should be stated at the outset that this evaluation is analytical rather than experimental. A stability lobe diagram is strictly defined for the receptance at the tool tip, which includes the dynamics of the spindle, the tool holder and the tool. In the present setup, the freely moving side of the module carried neither a spindle nor a tool, so the measured FRFs describe the module together with its clamping, not a machining point. The diagrams presented below therefore illustrate how the stability boundary responds to a change of the angular position φ; they are not predictions of the stability limits of a particular machining operation, and they are not validated by cutting tests. Such a validation, carried out on an MRMT configuration in which the module is located in the force flow between the spindle and the workpiece, is part of future work.

The following assumptions are made for the SLD computation. Each assumption is stated together with its effect on the resulting stability boundary.

- *Truncation order $r = 0$:* Only the average component of the Fourier expansion is retained, which is the most simplistic approximation in [49]. This is justified for the present analysis because the average cutting force per tooth

period is independent of the helix angle, so the resulting expression is valid for helical end mills as well [49]. The trade-off is that the accuracy of the predicted lobes degrades as the radial immersion is reduced; for radial immersions of only a few percent, the cutting force becomes more impulse-like and higher-order terms or time-domain methods would be required to capture all stability features [50]. As the present analysis is carried out at full radial immersion (slotting), this limitation does not apply here.

- *Worst-case milling condition – slotting:* Slotting (full-immersion milling) is selected as the cutting case because it is the most aggressive standard milling operation in terms of average chip load and continuous tooth engagement, and therefore yields the lowest chatter-free depth of cut. Lobe positions and the absolute chatter-free depth of cut obtained for slotting are thus a conservative bound for less demanding immersion conditions.

- *Tool and material parameters:* A four-fluted end mill ($N_t = 4$) with zero helix angle is assumed, in line with the geometric assumption of [49]. The tool-workpiece pair is characterized by a specific cutting force coefficient $K_s = 750\,\mathrm{N\,mm^{-2}}$ and a force angle $\beta = 75°$, both representative values for milling of aluminum alloys. Because the same parameter set is used for every φ, any change in the resulting SLD can unambiguously be attributed to the change of dynamic stiffness induced by the module.

- *One-dimensional* FRF *measurement:* The stiffness-adjustable module modifies the compliance only along a single axis, so the impact-hammer measurements presented in Figure 7 were carried out one-dimensionally. The Altintas & Budak formulation, however, requires FRFs in both the feed (X) and the normal (Y) direction. For the present analysis, the measured FRF is therefore used identically in both directions ($G_{xx}(j\omega) = G_{yy}(j\omega)$). This assumption is acceptable here because the goal is to isolate the effect of φ on the SLD: any anisotropy of the surrounding structure would be common to all six φ settings and would not change the relative shift of the lobes between them. Absolute values of a_{lim}, however, must be interpreted with this assumption in mind.

- *Accelerance instead of receptance, measured at the module:* As described in Section 5.2, the FRF was measured with an accelerometer attached directly to the stiffness-adjustable module, which yields the accelerance $A(j\omega) = \ddot{X}(j\omega)/F(j\omega)$ at this point. The Altintas & Budak formulation, in contrast, requires the receptance $G(j\omega) = X(j\omega)/F(j\omega)$ at the tool tip. The two are related by $G(j\omega) = -A(j\omega)/\omega^2$, so the conversion is straightforward; what is not straightforward is the location: the receptance at the tool tip would, in an integrated machine, additionally include the dynamics of the spindle, the tool holder and the tool. The SLDs presented here therefore describe how the stability boundary shifts due to the module alone, not absolute stability limits of a complete machining setup. A further consequence of this conversion is that contributions well below the module frequency are weighted by ω^{-2} relative to the module mode. As shown in this section, this is the reason why absolute depth-of-cut values cannot be evaluated from the present measurement.

The resulting SLDs are shown in Figure 9. The stability lobes shift along the spindle-speed axis as φ is varied, following the frequency of the module mode reported in Figure 7(b). Between $\varphi = 40°$ and $\varphi = 50°$ the lobes shift back towards higher spindle speeds, consistent with the local departure from the stiffness-governed trend discussed in Section 5.2.

The absolute chatter-free depth of cut is not evaluated here. The FRFs used for the SLD computation were measured on the module clamped in a vice and contain, besides the module mode, further poles at every angular position, including poles below the module mode between 24 Hz to 66 Hz. The conversion from the measured accelerance to the receptance required by the Altintas and Budak formulation scales with ω^{-2} and therefore weights contributions below the module mode more strongly than the module mode itself. As a consequence, the minimum of $a_{\mathrm{lim}}(n)$ is not governed by the module: at none of the six angular positions does the minimum of the real part of the oriented FRF occur close to the identified module frequency. Restricting the evaluated frequency band does not resolve this, since the resulting value of $a_{\mathrm{lim,abs}}$ then depends on the chosen band limits rather than on the

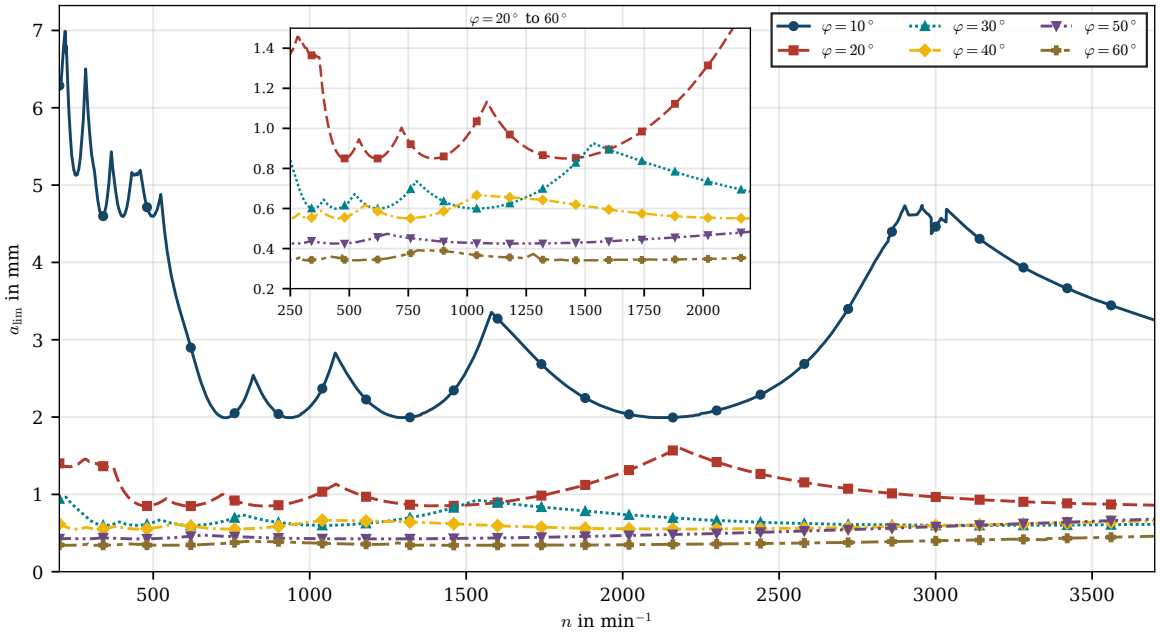


Figure 9: Stability lobe diagrams computed from the measured FRFs of the stiffness-adjustable module ($T = 5\,\mathrm{mm}$) for each of the six angular positions $\varphi \in \{10°, 20°, 30°, 40°, 50°, 60°\}$. The cutting case is full-radial-immersion slotting with $N_t = 4$, $K_s = 750\,\mathrm{N\,mm^{-2}}$ and $\beta = 75°$. For each curve, the area below the curve corresponds to chatter-free cutting conditions. The diagrams are evaluated with respect to the position of the lobes along the spindle-speed axis; the absolute level of a_{lim} is governed by resonances of the clamping rather than by the module and is not interpreted here (see Section 5.2.1).

module configuration; for lower band limits between 65 Hz to 85 Hz it varies by up to 70 % at $\varphi = 60°$ and by 43 % at $\varphi = 50°$. The SLDs presented here are therefore evaluated with respect to the position of the stability lobes along the spindle-speed axis, which follows the module mode, and not with respect to absolute depth-of-cut values. Determining the latter would require a setup in which the module is the compliant element of the measured structure, which is proposed as future work.

For a given spindle speed and depth of cut, the change of φ therefore shifts the lobe pattern relative to the operating point, so that an operating point located in an unstable region for one angular position can fall into a stable region for another. This shows that the proposed module enables an in-situ adaptation of the stability boundaries of the milling process and is therefore a suitable hardware element for process-driven reconfiguration of MRMT.

6. Discussion

The two analyses presented in Section 5 are now discussed with respect to the two research questions formulated in Section 2.3.

6.1. Length-adjustable feed axis

To classify the achieved accuracy against industrial practice, Table 2 places the measured geometric deviations in context (discussed below). The measurements show that travel-range extension at the module level is feasible without sacrificing the order of magnitude of accuracy expected from a feed axis: the maximum straightness deviation observed across the full extended travel range is 175.88 µm, the rotational deviations stay within 0.1°, and forward and backward runs agree with an NRMSE of 0.0236. The decisive observation, however, is not the absolute value but the spatial structure of the deviations: straightness deviation varies sinusoidally along the extension segments with a peak-to-peak period equal to the length of one extension segment, while the roll deviation varies across the segment interfaces. The dominating contributor is therefore the assembly interface between segments rather than the rack-pinion gap or backlash. This finding is the answer to the first research question: at the module level, the limit of travel-range extension in the present MRMT concept is set by the geometric quality of the segment interface.

Table 2: Industrial classification of the measured geometric accuracy of the length-adjustable feed axis. Values are characteristic magnitudes over the 470 mm travel. The compared quantities differ in type (straightness vs. positioning accuracy vs. workpiece tolerance) and are intended as an order-of-magnitude reference only.

Reference	**Characteristic deviation**
This work, base segment	straightness 2.05 µm to 44.5 µm; angular $\leq 0.10°$ (max. component: Yaw)
This work, extension segments	straightness 6.76 µm to 175.88 µm; angular $\leq 0.068°$ (max. component: Pitch)
General workpiece tol. (ISO 2768-f / -m, 400 mm to 1000 mm) [51]	±300 µm / ±800 µm
Industrial rack-and-pinion axis (premium) [52]	machine precision $\approx$ 1 µm to 20 µm; rack cumulative pitch error 12 µm to 15 µm

The measured deviations are assessed against the general workpiece tolerances of ISO 2768 [51], which express the accuracy a machined part typically requires, and against the geometric and positioning accuracy of established CNC feed axes, which represents the state of the art. The maximum straightness deviation of 175.88 µm stays within ISO 2768-medium (±800 µm at the relevant length scale) by a factor of about 4.5, but within ISO 2768-fine (±300 µm) only by a factor of about 1.7, which leaves little margin for other error sources of the machining process. Relative to precision milling centres, whose positioning uncertainty and straightness lie in the single-digit to low-tens-of-micrometre range, the prototype is roughly one order of magnitude coarser in translation and one to two orders coarser in the angular error motions. The axis therefore classifies as a coarse- or workshop-positioning axis, suited to roughing and large-structure machining rather than precision finishing. This gap is, however, not inherent to the length-adjustable principle: as shown above, the dominant error source is the end-face flatness of the segment interfaces and the resulting alignment, which face milling, tapered or kinematic interfaces, and error compensation can reduce without altering the modular concept.

When assembling the length-adjustable feed axis, the primary focus is on the alignment of the length-extending segments. In the proposed design, the stiffness at the segment interfaces is adjusted by tightening the bolt connectors, which in turn strongly influences the alignment of the segments: the achievable alignment is governed by the manufacturing accuracy, in particular the flatness of the aluminum profile end faces, and the observed straightness deviations can be traced back to insufficient end-face flatness. The forward/backward consistency reported in Section 5.1 suggests that neither backlash nor the rack gap contributes significantly. With the proposed design, deviations in straightness appear gradually rather than instantaneously because the carriage length is twice the length of a single extension segment; the resulting periodicity of the straightness deviation should be considered in future compensation strategies. For more accurate alignment, we recommend face milling the ends of the aluminum profiles to tight tolerances. Another potential solution is to design the end faces with a tapered shape, similar to steep taper tool holders; further research should investigate such tapered interfaces, as they may allow for more accurate and easier alignment of the extension segments.

Another crucial point that significantly affects accuracy is the alignment of the linear guides to each other. The surfaces on which the linear guides are mounted must be dimensioned to match the face-milled ends of the aluminum profiles to ensure consistent alignment. A significant variation in the yaw angle was observed for the long base segment (Max – Min = 0.101°, markedly larger than 0.056° on the extension segments), which can be attributed to assembly and alignment constraints: The height of the base plate was limited due to the way the rack and pinion drive had to be mounted. As a result, the lateral mounting surfaces for the linear guides were designed to be low in height, making precise lateral alignment more challenging. This misalignment is a potential contributor to the observed yaw variations. Similarly, the pitch behavior differs between the two segments – decreasing noticeably along the travel distance within the base segment (Max – Min = 0.042°), but increasing along the travel distance within the extension segments (Max – Min = 0.068°, i.e. approximately 62 % larger) – which can be related to alignment errors during assembly: the aluminum profiles were cut, resulting in imperfectly perpendicular interfaces with respect to the mounting surfaces of the base plates, which propagates through the linear guide alignment.

All measurements presented here were taken on a single assembly of the axis. How far the ob-

served deviations reproduce after disassembly and reassembly of the segments was not investigated. This is essential for the compensation strategies mentioned above: if a compensation has to be re-identified after every reconfiguration, the required measurement effort adds to the ramp-up time of the reconfigured MRMT. The reassembly repeatability of the segment interfaces should therefore be quantified in future work.

In conclusion, to improve the overall performance of the length-adjustable feed axis, future work should focus on:

- Refinement of the segment interfaces: Investigate tapered end face geometries to improve alignment accuracy.
- Compensation strategies: Implement correction algorithms based on the predictable nature of the straightness errors.
- Optimize assembly techniques: Develop more robust alignment procedures to reduce error propagation between segments.

6.2. Stiffness-adjustable module

The measurements answer the second research question of this paper directly: the chatter stability of a milling process can be tuned within a single mechanical interface module by varying its stiffness. Three observations support this conclusion. First, the static stiffness varies between $644.47\,\mathrm{N\,mm^{-1}}$ ($T = 4\,\mathrm{mm}$, $\varphi = 60°$) and $2613.93\,\mathrm{N\,mm^{-1}}$ ($T = 5\,\mathrm{mm}$, $\varphi = 10°$), demonstrating that the static behavior of the module spans a wide range. Second, the dynamic behavior is consistent with an SDOF representation driven by the measured static stiffness: the identified module mode shifts by 56.45 %, from 96.09 Hz at $\varphi = 60°$ to 220.66 Hz at $\varphi = 10°$ for $T = 5\,\mathrm{mm}$. Compared to Hansmann et al. [38], the operating bandwidth is extended by about 61 % (from 137 Hz to 220.66 Hz), bringing it into the range relevant for milling processes. Third, and most important for the MRMT property under investigation, this dynamic shift propagates to the chatter stability boundary: the stability lobes move along the spindle-speed axis as φ is varied. The dynamic adjustment of a single interface module is therefore sufficient to actively reposition the stability boundary of the milling process.

The comparison between static and dynamic behavior is subject to one limitation that follows from the two test setups. The static stiffness was determined from a compression test up to the nominal load of 5 kN applied with a hand press, and therefore represents a secant stiffness over the full load range, whereas the impact-hammer tests were carried out on the freely vibrating, unloaded module and probe the tangent stiffness around the unloaded state. These two quantities are not necessarily equal. The spring plate is preloaded and the pins slide in their contacts, so the force-displacement behavior is not linear, and the ratio between the two stiffness values may itself change with φ. The scaling parameter f_s of the SDOF model absorbs a constant offset between them but not a φ-dependent one, and part of the residual scatter of the model, as well as the spread of the back-calculated modal mass, is plausibly attributable to this effect. A characterization of the dynamic behavior under representative static preload is therefore proposed as future work.

The bidirectional force transmission realized in the module additionally lifts a structural restriction of the original mechanism by Hansmann et al. [38], which allowed force transmission only in one spatial direction. This change is not the focus of this paper but is a prerequisite for using the module as a generic mechanical interface in an MRMT, where forces in both positive and negative spatial directions occur. It should be noted, however, that the static stiffness was characterized in compression only; a dedicated characterization of the tensile load path via the central screw remains open and should be part of future work. A practical limitation of the current implementation is that changing the spring plate thickness T requires manual disassembly. For the goal of automated reconfiguration this is a drawback that should be addressed in future work, for instance by integrating an actuated stack of spring plates.

Since the frequency model requires only a single scaling parameter on top of the static stiffness regression, it remains simple enough to be implemented in control or edge devices. This approach is limited to the first natural frequency, which often has the most influence on process quality, e.g. chatter. More involved approaches, e.g. Gaussian process regression or finite element analysis [53, 54] are more precise over the whole frequency band, however are more computationally intensive. The models obtained can be used in the future for a control system that can adjust the process's natural frequencies to the required specifications.

The process-side evaluation in Section 5.2.1 shows that the change of dynamic stiffness induced by φ does not only manifest itself in the FRF, but also in a measurable shift of the chatter stability boundary of a representative milling process. Two implications follow from this. First, for a given milling process with fixed spindle speed and tool, the operating point can be moved into a chatter-free region by selecting a suitable φ. Second, the regression models for the natural frequency and the static stiffness can be combined with the analytical SLD computation in a feed-forward control scheme. Such a scheme would, given a target spindle speed and depth of cut, output the angular position φ that maximizes process stability. The implementation of such a closed-loop process-stability controller and its experimental validation in a real milling process are subject to future work. A further limitation of the present analysis is that the SLDs are based on the FRFs measured on the isolated module clamped in a vice. As shown in Section 5.2.1, the resonances of the clamping govern the minimum of the limiting depth of cut, so that only the position of the stability lobes, and not their absolute level, can be attributed to the module. A meaningful evaluation of absolute stability limits requires a setup in which the module is the compliant element of the measured structure; in an integrated MRMT configuration, the dynamics of the surrounding structure will additionally contribute to the system response and the resulting SLDs.

7. Conclusion

This study analyzed how the travel range of a feed axis and the chatter stability of a milling process can be adapted at the module level. The analysis was carried out on two purpose-built hardware platforms: a length-adjustable rack-and-pinion feed axis and a stiffness-adjustable mechanical interface module.

- *Workspace adaptation.* Extending the feed axis at the module level keeps the maximum straightness deviation at 175.88 µm and the rotational deviations within 0.1° across base and extension segments. The deviations along the extended axis are dominated by the assembly interface between segments rather than by the rack-pinion gap or backlash: straightness deviation varies sinusoidally with a period corresponding to the length of an extension segment, and the roll deviation varies across the segment interfaces. The pitch variation was larger on the extension segments (Max – Min = 0.068°) than on the base segment (Max – Min = 0.042°), about 62 % larger. The geometric quality of the segment interface is therefore identified as the primary limit of intra-module travel-range extension and as the main lever for further improvement, e.g. through tapered interfaces and face-milled end-faces, as well as integrated metrology.

- *Process-stability adaptation:* Varying the angular position φ of the stiffness-adjustable interface module changes the static stiffness between $644.47\,\mathrm{N\,mm^{-1}}$ and $2613.93\,\mathrm{N\,mm^{-1}}$ (across both spring plate thicknesses) and shifts the dominant natural frequency of the module by 56.45 %, from 96.09 Hz to 220.66 Hz. Stability lobe diagrams derived from the measured FRFs for each φ show that this dynamic adjustability propagates to the milling process: the lobe positions along the spindle-speed axis change with φ. A previously unstable operating point can therefore be moved into the chatter-free region by selecting a suitable φ, which establishes the module as a hardware element for in-situ adaptation of the process stability boundaries in MRMT.

Funding

This work is funded by the German Research Foundation (DFG)-SFB 1574-471687386.

Data availability statement

The data that support the findings of this study are available from the corresponding author, F. H., upon reasonable request.

Declaration of competing interest

The authors declare that they have no known competing financial interests or personal relationships that could have appeared to influence the work reported in this paper.

CRediT authorship contribution statement

Fabian Heimberger: Conceptualization, Data curation, Formal analysis, Investigation, Methodology, Project administration, Software, Validation, Visualization, Writing – original draft, Writing – review & editing. **Max Goebels:** Conceptualization, Data curation, Formal analysis, Investigation, Methodology, Project administration, Software, Validation, Visualization, Writing – original draft, Writing – review & editing. **Jakob Janzen:** Conceptualization, Formal analysis, Investigation, Methodology, Visualization, Writing – original draft. **Manuel Bader:** Conceptualization, Formal analysis, Investigation, Methodology, Visualization, Writing – original draft. **Alexander Puchta:** Funding acquisition, Resources, Supervision, Writing – review & editing. **Florian Oexle:** Methodology, Funding acquisition, Resources, Supervision, Writing – review & editing. **Jürgen Fleischer:** Funding acquisition, Project administration, Resources, Supervision, Writing – review & editing.

Abbreviations

DOF	degree of freedom
FRF	frequency response function
MAC	Modal Assurance Criterion
MPE	maximum permissible error
MRMT	modular reconfigurable machine tools
NRMSE	Normalized Root Mean Squared Error
SDM	software-defined manufacturing
SDOF	single degree of freedom
SLD	stability lobe diagram

References

[1] E. Westkämper, C. Löffler, Strategien der Produktion: Technologien, Konzepte und Wege in die Praxis, 1st Edition, Springer, Berlin, 2016. doi:10.1007/978-3-662-48914-7.

[2] M. G. Mehrabi, A. G. Ulsoy, Y. Koren, P. Heytler, Trends and perspectives in flexible and reconfigurable manufacturing systems, Journal of Intelligent Manufacturing 13 (2) (2002) 135–146. doi:10.1023/A:1014536330551.

[3] A. Molina, C. A. Rodriguez, H. Ahuett, J. A. Cortés, M. Ramírez, G. Jiménez, S. Martinez, Next-generation manufacturing systems: key research issues in developing and integrating reconfigurable and intelligent machines, International Journal of Computer Integrated Manufacturing 18 (7) (2005) 525–536. doi:10.1080/09511920500069622.

[4] C. Renzi, F. Leali, M. Cavazzuti, A. O. Andrisano, A review on artificial intelligence applications to the optimal design of dedicated and reconfigurable manufacturing systems, The International Journal of Advanced Manufacturing Technology 72 (1) (2014) 403–418. doi:10.1007/s00170-014-5674-1.

[5] L. N. Pattanaik, P. K. Jain, N. K. Mehta, Cell formation in the presence of reconfigurable machines, The International Journal of Advanced Manufacturing Technology 34 (3) (2007) 335–345. doi:10.1007/s00170-006-0592-5.

[6] L. Benyoucef (Ed.), Reconfigurable Manufacturing Systems: From Design to Implementation, Springer Series in Advanced Manufacturing, Springer International Publishing, Cham, 2020.

[7] Y. Koren, The Global Manufacturing Revolution: Product-Process-Business Integration and Reconfigurable Systems, 1st Edition, John Wiley & Sons, Inc., Hoboken, New Jersey, 2010. doi:10.1002/9780470618813.

[8] E. Mühlbeier, P. Gönnheimer, L. Hausmann, J. Fleischer, Value Stream Kinematics, in: B.-A. Behrens, A. Brosius, W. Hintze, S. Ihlenfeldt, J. P. Wulfsberg (Eds.), Production at the leading edge of technology, Springer, Berlin, Heidelberg, 2021, pp. 409–418. doi:10.1007/978-3-662-62138-7_41.

[9] T. Arndt, V. Schulze, T. Bertram, M. Bryg, M. Kipfmüller, J. Kotschenreuther, Drehen mit dem Roboter und mehreren Werkzeugen/Turning with a robot and several tools, wt Werkstattstechnik online 112 (10) (2022) 722–726. doi:10.37544/1436-4980-2022-10-92.

[10] E. Mühlbeier, F. Oexle, E. Gerlitz, N. Matkovic, P. Gönnheimer, J. Fleischer, Conceptual control architecture for future highly flexible production systems, Procedia CIRP 106 (2022) 39–44. doi:10.1016/j.procir.2022.02.152.

[11] T. Cvitanic, V. Nguyen, S. N. Melkote, Pose optimization in robotic machining using static and dynamic stiffness models, Robotics and Computer-Integrated Manufacturing 66 (2020) 101992. doi:10.1016/j.rcim.2020.101992.

[12] F. Frick, C. Ellwein, A. Lechler, M. Neubauer, A. Verl, Software-Defined Manufacturing: Reference Architecture, in: 2024 International Symposium on Power Electronics, Electrical Drives, Automation and Motion (SPEEDAM), 2024, pp. 1289–1295. doi:10.1109/SPEEDAM61530.2024.10609236.

[13] A. Lechler, C. Kircher, A. Verl, SDM – Software Defined Manufacturing*/SDM – Software Defined Manufacturing, wt Werkstattstechnik online 108 (05) (2018) 307–312. doi:10.37544/1436-4980-2018-05-33.

[14] F. Jaensch, A. Csiszar, C. Scheifele, A. Verl, Digital Twins of Manufacturing Systems as a Base for Machine Learning, in: 2018 25th International Conference on Mechatronics and Machine Vision in Practice (M2VIP), 2018, pp. 1–6. doi:10.1109/M2VIP.2018.8600844.

[15] M. Goebels, A. Schulte, P. Georgi, F. Heimberger, J. Schwalm, O. Liewerenz, A. Schäfer, J. Fleischer, A. Verl, H.-C. Möhring, V. Schulze, S. Matthiesen, N. Parspour, Software-Defined Value Stream Process Systems, Machines 13 (1) (2025) 42. doi:10.3390/machines13010042.

[16] T. Stehle, U. Heisel, Konfiguration und Rekonfiguration von Produktionssystemen, in: D. Spath, E. Westkämper, H.-J. Bullinger, H.-J. Warnecke (Eds.), Neue Entwicklungen in der Unternehmensorganisation, Springer Berlin Heidelberg, Berlin, Heidelberg, 2017, pp. 333–367.

[17] J. Padayachee, G. Bright, Modular machine tools: Design and barriers to industrial implementation, Journal of Manufacturing Systems 31 (2) (2012) 92–102. doi:10.1016/j.jmsy.2011.10.003.

[18] Y. Koren, X. Gu, W. Guo, Reconfigurable manufacturing systems: Principles, design, and future trends, Frontiers of Mechanical Engineering 13 (2) (2018) 121–136. doi:10.1007/s11465-018-0483-0.

[19] M. Gadalla, D. Xue, Recent advances in research on reconfigurable machine tools: a literature review, International Journal of Production Research 55 (5) (2017) 1440–1454. doi:10.1080/00207543.2016.1237795.

[20] Z. Xu, F. Xi, L. Liu, L. Chen, A Method for Design of Modular Reconfigurable Machine Tools, Machines 5 (1) (2017) 5. doi:10.3390/machines5010005.

[21] T. Lorenzer, Wandelbarkeit in der Serienfertigung durch rekonfigurierbare Werkzeugmaschinen, Züricher Schriften zur Produktionstechnik - IWF - Institut für Werkzeugmaschinen und Fertigung 199 (2011). doi:10.3929/ethz-a-006381940.

[22] Z. M. Bi, Development and Control of a 5-Axis Reconfigurable Machine Tool, Journal of Robotics 2011 (1) (2011) 583072. doi:10.1155/2011/583072.

[23] B. Peukert, M. Saoji, E. Uhlmann, An Evaluation of Building Sets Designed for Modular Machine Tool Structures to Support Sustainable Manufacturing, Procedia CIRP 26 (2015) 612–617. doi:10.1016/j.procir.2014.07.175.

[24] E. Uhlmann, M. Saoji, B. Peukert, Principles for Interconnection of Modular Machine Tool Frames, Procedia CIRP 40 (2016) 413–418. doi:10.1016/j.procir.2016.01.081.

[25] E. Uhlmann, B. Peukert, Reconfiguring machine tool behavior via smart building block systems, Procedia Manufacturing 28 (2019) 127–134. doi:10.1016/j.promfg.2018.12.021.

[26] E. Uhlmann, M. Polte, J. Blumberg, B. Peukert, 3-Achs-Portalfräsmaschine als Demonstrator für ein modulares Werkzeugmaschinengestell, Zeitschrift für wirtschaftlichen Fabrikbetrieb 114 (9) (2019) 545–548. doi:10.3139/104.112141.

[27] M. M. Hausladen, B. Zhao, M. S. Kubala, L. F. Francis, T. M. Kowalewski, C. J. Ellison, Synthetic growth by self-lubricated photopolymerization and extrusion inspired by plants and fungi, Proceedings of the National Academy of Sciences 119 (33) (2022) e2201776119. doi:10.1073/pnas.2201776119.

[28] H. Liang, Y. Wu, Y. Zhang, E. Chen, Y. Wei, Y. Ji, Elastomers Grow into Actuators, Advanced Materials 35 (12) (2023) 2209853. doi:10.1002/adma.202209853.

[29] S. Al Harthy, S. M. H. Sadati, C. Girerd, S. Kim, A. Mondini, Z. Wu, B. Saldarriaga, C. A. Seneci, B. Mazzolai, T. K. Morimoto, C. Bergeles, Tip-Growing Robots: Design, Theory, Application, IEEE Transactions on Robotics 41 (2025) 5511–5532. doi:10.1109/TRO.2025.3608701.

[30] P. Li, Y. Zhang, J. Quan, G. Zhang, D. Zhou, L. Li, Enhanced Deformation Resistance and Load-Bearing Capacity in Tip-Growing Robots Through Scale-Inspired Layer Jamming Mechanism, Soft Robotics 12 (6) (2025) 732–741. doi:10.1089/soro.2024.0147.

[31] C. Brecher, M. Weck, Werkzeugmaschinen Fertigungssysteme, Springer, Berlin, Heidelberg, 2017.

[32] C. Yue, H. Gao, X. Liu, S. Y. Liang, L. Wang, A review of chatter vibration research in milling, Chinese Journal of Aeronautics 32 (2) (2019) 215–242. doi:10.1016/j.cja.2018.11.007.

[33] J. Burtscher, J. Fleischer, Adaptive tuned mass damper with variable mass for chatter avoidance, CIRP Annals 66 (1) (2017) 397–400. doi:10.1016/j.cirp.2017.04.059.

[34] I. K. Kuder, A. F. Arrieta, W. E. Raither, P. Ermanni, Variable stiffness material and structural concepts for morphing applications, Progress in Aerospace Sciences 63 (2013) 33–55. doi:10.1016/j.paerosci.2013.07.001.

[35] Q. Wang, G. Senatore, K. Jansen, A. Habraken, P. Teuffel, Design and characterization of variable stiffness structural joints, Materials & Design 187 (2020) 108353. doi:10.1016/j.matdes.2019.108353.

[36] N. Govindan, S. Ramesh, A. Thondiyath, Design of a Variable Stiffness Joint Module to Quickly Change the Stiffness and to Reduce the Power Consumption, IEEE Access 8 (2020) 138318–138330. doi:10.1109/ACCESS.2020.3012031.

[37] C. Yuan Lin, J. Pin Hung, T. Liang Lo, Effect of preload of linear guides on dynamic characteristics of a vertical column–spindle system, International Journal of Machine Tools and Manufacture 50 (8) (2010) 741–746. doi:10.1016/j.ijmachtools.2010.04.002.

[38] J. Hansmann, W. Kaal, B. Seipel, T. Melz, Einstellbares Federelement für Adaptierbaren Schwingungstilger, ATZ - Automobiltechnische Zeitschrift 114 (3) (2012) 242–247. doi:10.1365/s35148-012-0295-1.

[39] J. Munoa, M. Zatarain, I. Bediaga, R. Lizarralde, Optimization of Hard Material Roughing by means of a Stability Model, in: 8th CIRP International Workshop on Modelling of Machining Operations, Chemnitz, Germany, 2005, pp. 431–438.

[40] Y. Altintas, J. H. Ko, Chatter Stability of Plunge Milling, CIRP Annals 55 (1) (2006) 361–364. doi:10.1016/S0007-8506(07)60435-1.

[41] C. Brecher, M. Weck, Werkzeugmaschinen Fertigungssysteme 3: Mechatronische Systeme, Steuerungstechnik und Automatisierung, Springer, Berlin, Heidelberg, 2021.

[42] Y. Altintas, A. Verl, C. Brecher, L. Uriarte, G. Pritschow, Machine tool feed drives, CIRP Annals 60 (2) (2011) 779–796. doi:10.1016/j.cirp.2011.05.010.

[43] Wittenstein alpha GmbH, Operating Manual alpha Rack and Pinion System (2022).

[44] International Organization for Standardization, ISO 230-1:2012, Test code for machine tools – Part 1: Geometric accuracy of machines operating under no-load or quasi-static conditions (2012).

[45] International Organization for Standardization, ISO 230-2:2014, Test code for machine tools – Part 2: Determination of accuracy and repeatability of positioning of numerically controlled axes (2014).

[46] Leica Geosystems AG, Leica AT930/AT960 User Manual (2022).

[47] S. Goldman, Vibration spectrum analysis: a practical approach, 1st Edition, Industrial Press Inc., New York, 1991.

[48] B. Peeters, H. Van Der Auweraer, P. Guillaume, J. Leuridan, The PolyMAX Frequency-Domain Method: A New Standard for Modal Parameter Estimation?, Shock and Vibration 11 (3-4) (2004) 395–409. doi:10.1155/2004/523692.

[49] Y. Altintas, E. Budak, Analytical Prediction of Stability Lobes in Milling, CIRP Annals 44 (1) (1995) 357–362. doi:10.1016/S0007-8506(07)62342-7.

[50] T. L. Schmitz, K. S. Smith, Machining Dynamics: Frequency Response to Improved Productivity, 2nd Edition, Springer International Publishing, Cham, 2019. doi:10.1007/978-3-319-93707-6.

[51] International Organization for Standardization, ISO 2768-1:1989, General tolerances – Part 1: Tolerances for linear and angular dimensions without individual tolerance indications (1989).

[52] WITTENSTEIN alpha GmbH, alpha rack & pinion system: Product catalog, Tech. rep., WITTENSTEIN alpha GmbH, Igersheim, Germany, machine precision and rack pitch-error data (Premium/Value/Smart Class) (2022).

[53] C. E. Rasmussen, C. K. I. Williams, Gaussian Processes for Machine Learning, The MIT Press, 2005. doi:10.7551/mitpress/3206.001.0001.
URL https://direct.mit.edu/books/oa-monograph/2320/Gaussian-Processes-for-Machine-Learning

[54] Y. Altintas, C. Brecher, M. Weck, S. Witt, Virtual Machine Tool, CIRP Annals 54 (2) (2005) 115–138. doi:10.1016/S0007-8506(07)60022-5.